ENCYCLOPEDIA OF

# SMART MATERIALS

## VOLUME 1

**Mel Schwartz**

The *Encyclopedia of Smart Materials* is available Online at
www.interscience.wiley.com/reference/esm

A Wiley-Interscience Publication
**John Wiley & Sons, Inc.**

## CONCLUSIONS

To maintain the technological lead in the area of advanced materials, manufacturing industries are well advised to build on the quantitative knowledge of the relationships between materials properties and processes. The development of advanced models for manufacturing systems must be done in parallel with advances in sensor and control technology. Whereas a model provides an understanding on the physics and chemistry involved, and explains the relationship between dependent and control variables, sensors provide information related to the state of the material and process variables. The control function maintains quality through the use of data provided by sensors as inputs to the models, and manages the process to achieve the desired product.

Pioneering efforts have proved the feasibility of the IPM concepts, both for advanced composites and metallic materials. Among the benefits for composite materials are the reductions of development costs and lead times, the enhancement of quality and reliability, and a simplification of the qualification procedures. For metallic materials, most of the experiences are concentrated on consolidation of intermetallic powders, but other processes such as forging and soldering are also investigated. In either case, the availability of affordable sensors is the critical issue for its industrial implementation.

## BIBLIOGRAPHY


1. *www.msel.nist.gov*
2. S.R. LeClair and A. Jackson., *Work Unit Directive (WUD54) Amendment: Materials Process Design*. NASA 19980069695 (1996).
3. *www.foxboro.com*
4. *www.ipm.virginia.edu*
5. *www.ipc.northwestern.edu*
6. *www.ccm.udel.edu*
7. *http://mining.ubc.ca/ipm*
8. A.C. Loos and G. Springer. J. *Compos. Mater.* **21**: 243–261 (1983).
9. L.A. Berglund and J.M. Kenny. *SAMPE J.* **27**(2): (1991).
10. S.G. Advani and P. Simacek. In *Resin Transfer Moulding for Aerospace Sciences*. Kluwer Academic, Dordrecht, Netherlands, 1998, pp. 225–281.
11. F. Rodríguez-Lence, P. Muñoz-Esquer, J.M. Menéndez, C. Pardo de Vera, S. Díaz, and J.A. Güemes. In *Proc. 12th Int. Conf. on Composite Materials,* ICCM-12, Paris, France, 1999.
12. C.W. Lee and B.P. Rice. *SAMPE J.* **34**(6): (1998).
13. D.D. Shepard and K.R. Smith. *J. Therm. Anal.* **49**(1): 95–100 (1997).
14. G. Maistros, D. Bofilios, G. Cracknell, and A. Milburn. In *Proc. 19th Int. SAMPE Europe Conf. of the Society for the Advancement of Materials and Process Engineering*, Paris, 1998, pp. 733–743.
15. S. Cossins, M. Connell, B. Cross, et al. *Appl. Spectroscopy* **50** (7): 900–905 (1996).
16. P.A. Crosby, G.R. Powell, G.F. Fernando, C.M. France, R.C. Spooncer, and D.N. Waters. *Smart Mater. Struct.* **5**(4): 415–428 (1996).
17. Y.M. Liu, C. Ganesh, J.P.H. Steele, and J.E. Jones. *J. Compos. Mater.* **31**(1): 87–102 (1997).
18. J.L. Kardos, M.P. Dudukovic, and R. Dave. In Dusek, ed., *Advances in Polymer Science*. Springer Verlag, Berlin, 1986, pp. 101–124.
19. D.G. Backman, E.S. Rusell, D.Y. Wey, and Y. Pang. In *Proc. Symp. on Intelligent Processing of Materials*. Minerals, Metals and Materials Society, Warrendale, PA. 1989.
20. T.F. Zahrah, F. Charron, and N.M. Wereley. In *AIAA/ASME Structures, Structural Dynamics and Materials Conf.*, April. 1994, pp. 2315–2323.
21. H.N.G. Wadley. In *Smart Structures and Materials: Implications for Military Aircraft of New Generation*, 1996.
22. H.N.G. Wadley and R. Vancheeswaran. *J. Mater.* (Jan.) **1**: 19–30 (1998).
23. W.B. Li, M.F. Ashby, and K.E. Easterling. *Acta Metall.* **35**: 2831 (1987).


# INTELLIGENT SYNTHESIS OF SMART CERAMIC MATERIALS


MALGORZATA M. LENCKA
OLI Systems, Inc.
Morris Plains, NJ

RICHARD E. RIMAN
Rutgers University
Piscataway, NJ


## INTRODUCTION

In this article, we focus on the hydrothermal synthesis of smart ceramic materials that have a perovskite-type structure. Engineering, processing, properties, and applications of these materials are discussed in Smart Perovskites. Perovskite compounds have the general formula $ABO_3$, where the A cation is relatively large and of low valence (such as $Ba^{2+}$, $Sr^{2+}$, $Ca^{2-}$, $Pb^{2-}$, $La^{3-}$, $Sm^{3-}$, $Nd^{3-}$, $Bi^{3-}$, and $K^{+}$) and the B cation is relatively small (such as $Ti^{4-}$, $Zr^{4-}$, $Sn^{4-}$, $W^{6+}$, $Nb^{5+}$, $Ta^{5+}$, $Fe^{3-}$, $Mn^{3-}$, $Mg^{2-}$, $Zn^{2-}$, and $Ni^{2+}$).

Hydrothermal synthesis involves numerous simultaneous reactions between dissolved and solid species in an aqueous system to form anhydrous multicomponent oxides. Hydrothermal media may provide an effective reaction environment for synthesizing numerous smart ceramic materials from a variety of precursor reagents (e.g., water-soluble salts, hydroxides, oxides) in the form of polycrystalline solids (1–15), thin films (16–22), and single crystals (23–25).

In particular, phase-pure ceramic materials that have controlled stoichiometry and morphology can be hydrothermally synthesized in a single experimental step from simple and inexpensive precursors at moderate temperatures and pressures (26) far below those required for conventional techniques. To take advantage of the opportunities offered by hydrothermal synthesis, it is important to select a precursor system that is both reactive and cost-effective. However, the reactivity of a precursor system can be judged only by optimizing the processing variables such as reagent

(precursor) concentrations and ratios, pH, temperature, and pressure, which can be extremely time-consuming due to the large number of variables involved. To improve the efficiency of evaluating a precursor system, a comprehensive thermodynamic model that simulates hydrothermal reactions has been developed (27–29). This model is a part of the OLI software (30). Our simulation approach has been validated for numerous perovskite-type multicomponent oxide systems, which include alkaline-earth titanates and zirconates (11,13,15), lead titanate (12), various solid solutions of lead zirconate titanate (14), lead magnesium niobate (31), and lead zinc niobate (31). In this article, modeling and experimental validation of selected hydrothermal systems are presented.

## THERMODYNAMIC MODEL

Before using the thermodynamic model, we select candidate starting materials (i.e., an appropriate precursor system) for hydrothermal synthesis. The thermodynamic model is used subsequently to predict the concentrations and activities of both ionic and neutral species in multicomponent systems that may contain an aqueous phase, any number of solid phases, and, if necessary, a vapor and a nonaqueous liquid phase. The starting point for the equilibrium calculations in the hydrothermal system is the computing speciation in the system investigated. For this purpose, a realistic model of electrolyte systems is used. This model combines information about standard-state properties of all species of interest and a formulation for the excess Gibbs energy, which accounts for the solution nonideality. The model has been described in detail by Rafal et al. (27) and Zemaitis et al. (28).

In a multicomponent system, the partial molal Gibbs energy of the $i$th species is related to the molality ($m_i$) by

$$\overline{G}_i = \overline{G}_i^0 + RT \ln m_i \gamma_i, \tag{1}$$

where $\overline{G}_i^0$ is the standard-state partial Gibbs energy and $\gamma_i$ is the activity coefficient. Thus, the thermodynamic properties of the system can be calculated if the standard-state Gibbs energies are available for all species as functions of temperature and pressure [i.e., $\overline{G}_i^0(T, P)$] and the activity coefficients are known as functions of the composition vector $m$ and temperature [i.e., $\gamma_i(m, T)$]. From basic thermodynamics, the standard-state Gibbs energy of formation $\overline{G}_i^0(T, P)$ can be calculated as a function of temperature and pressure if the following data are available:

1. Gibbs energy of formation at a reference temperature and pressure (usually $T_r = 298.15$ K and $P_r = 1$ bar),
2. enthalpy of formation at $T_r$ and $P_r$,
3. entropy at $T_r$ and $P_r$,
4. heat capacity as a function of temperature and pressure, and
5. volume as a function of temperature and pressure.

The key to representing the standard-state properties across substantial temperature and pressure ranges is accurate knowledge of the heat capacity and volume. The Helgeson–Kirkham–Flowers–Tanger equation of state (32,33) is used for this purpose. This equation accurately represents the standard-state thermodynamic functions of aqueous, ionic, and neutral species as functions of both temperature and pressure. In its revised form (33), the HKFT equation can reproduce the standard-state properties up to 1000°C and 5 kbar.

The HKFT equation is based on solvation theory and expresses the standard-state thermodynamic functions as sums of structural and solvation contributions, the latter depend on the properties of the solvent (i.e., water). The standard partial molal volume ($\overline{V}^0$) and heat capacity ($\overline{C}_p^0$) are given by

$$\overline{V}_0 = a_1 + \frac{a_2}{\Psi + P} + \left(a_3 + \frac{a_4}{\Psi + P}\right)\left(\frac{1}{T - \Theta}\right) - \omega Q + \left(\frac{1}{\varepsilon} - 1\right)\left(\frac{\partial \omega}{\partial P}\right)_T, \tag{2}$$

$$\overline{C}_p^0 = c_1 + \frac{c_2}{(T - \Theta)^2} - \left[\frac{2T}{(T - \Theta)^3}\right] \times \left[a_3(P - P_r) + a_4 \ln \frac{\Psi + P}{\Psi + P_r}\right] + \omega T X + 2TY\left(\frac{\partial \omega}{\partial T}\right)_P - T\left(\frac{1}{\varepsilon} - 1\right)\left(\frac{\partial^2 \omega}{\partial T^2}\right)_P, \tag{3}$$

where $a_1$, $a_2$, $a_3$, $a_4$, $c_1$, and $c_2$ represent species-dependent nonsolvation parameters, $T_r$ is the reference temperature of 298.15 K, $P_r$ is the reference pressure of 1 bar, and $\Psi$ and $\Theta$ refer to solvent parameters equal to 2600 bars and 228 K, respectively. $Q$, $X$, and $Y$ denote the Born functions given by

$$Q = \frac{1}{\varepsilon}\left(\frac{\partial \ln \varepsilon}{\partial P}\right)_T, \tag{4}$$

$$X = \frac{1}{\varepsilon}\left[\left(\frac{\partial^2 \ln \varepsilon}{\partial T^2}\right)_P - \left(\frac{\partial \ln \varepsilon}{\partial T}\right)_P^2\right], \tag{5}$$

$$Y = \frac{1}{\varepsilon}\left(\frac{\partial \ln \varepsilon}{\partial T}\right)_P, \tag{6}$$

where $\varepsilon$ is the dielectric constant of water and $\omega$ stands for the Born coefficient, which is defined for the $j$th aqueous species by

$$\omega_j \equiv \omega_j^{\text{abs}} - Z_j \omega_{\text{H}^+}^{\text{abs}}. \tag{7}$$

In Eq. (7), $Z_j$ is the charge on the $j$th aqueous species, $\omega_{\text{H}^+}^{\text{abs}}$ refers to the absolute Born coefficient of the hydrogen ion and $\omega_j^{\text{abs}}$ designates the absolute Born coefficient of the $j$th species given by

$$\omega_j^{\text{abs}} = \frac{N^0 e^2 Z_j^2}{2 r_{e,j}}, \tag{8}$$

where $N^0$ is the Avogadro number, $e$ is the electron charge, and $r_{e,j}$ denotes the effective electrostatic radius of the $j$th species, which is related to the crystallographic radius $r_{x,j}$

by

$$r_{e,j} = r_{x,j} + |z_j|(k_z + g), \tag{9}$$

where $k_z$ represents a charge-dependent constant equal to 0.0 for anions and 0.94 for cations and $g$ denotes a generalized function of temperature and density. Thus, the HKFT equation expresses the heat capacity and volume as functions of pure water properties and seven empirical parameters, which have been tabulated for large numbers of ions, complexes, and neutral inorganic and organic molecules. The remaining thermodynamic properties are obtained by thermodynamic integration using the values of the Gibbs energy, enthalpy, and entropy at reference temperature and pressure as integration constants.

The activity coefficient model used for representing the solution nonideality is an extended form of an expression developed by Bromley (34). The Bromley equation is a combination of the Debye–Hückel term for long-range electrostatic interactions and a semiempirical expression for short-range interactions between cations and anions. In a multicomponent system, the activity coefficient of an ion $i$ is given by

$$\log \gamma_i = \frac{-Az_i^2 I^{1/2}}{1 + I^{1/2}} + \sum_j^{NO} \left[\frac{|z_i| + |z_j|}{2}\right]^2 \times \left[\frac{(0.06 + 0.6B_{ij})|z_i z_j|}{\left(1 + \dfrac{1.5}{|z_i z_j|} I\right)^2} + B_{ij} + C_{ij} I + D_{ij} I^2\right] m_j, \tag{10}$$

where $A$ is the Debye–Hückel coefficient which depends on temperature and solvent properties; $z_i$ is the number of charges on ion $i$; $I$ is the ionic strength (i.e., $I = 0.5 \sum z_i^2 m_i$); $NO$ is the number of ions whose charges are opposite to that of ion $i$; and $B_{ij}$, $C_{ij}$, and $D_{ij}$ are empirical, temperature-dependent cation–anion interaction parameters. Bromley's (34) original formulation contains only one interaction parameter, $B_{ij}$, which is sufficient for systems of moderate ionic strength. For concentrated systems, the two additional coefficients $C_{ij}$ and $D_{ij}$ usually become necessary. The three-parameter form of the Bromley model can reproduce activity coefficients in solutions whose ionic strength is up to 30 mol/kg $H_2O$. The temperature dependence of the $B_{ij}$, $C_{ij}$, and $D_{ij}$ parameters is usually expressed by a simple quadratic function.

The Bromley model is restricted to interactions between cations and anions. For ion–molecule and molecule–molecule interactions, the well-known model of Pitzer (35) is used. To calculate the fugacities of components in the gas phase, the Redlich–Kwong–Soave (36) equation of state is used.

In the absence of sufficient experimental data, reasonable predictions can be made using a method due to Meissner (37) that makes it possible to extrapolate the activity coefficients to higher ionic strengths based on only a single, experimental or predicted, data point.

## Computational Method

The thermodynamic model is formulated for $k$ independent reactions. The $j$th reaction ($j = 1, \ldots, k$) can be written as

$$\sum_{i=1}^{n_j} \nu_i^{(j)} A_i^{(j)} = 0, \qquad j = 1, \ldots, k, \tag{11}$$

where $A_i^{(j)}$ is the $i$th chemical species participating in the $j$th reaction, $\nu_i^{(j)}$ is the stoichiometric number of species $A_i^{(j)}$, and $n_j$ is the total number of species undergoing the $j$th reaction.

The equilibrium state of the $j$th reaction is defined by the standard Gibbs energy change of the reaction

$$\Delta G_j^\circ = \sum_{i=1}^{n_j} \nu_i^{(j)} \Delta G_f^\circ\left(A_i^{(j)}\right) = -RT \ln K_j(T, P), \qquad j = 1, \ldots, k, \tag{12}$$

where $\Delta G_f^\circ(A_i^{(j)})$ is the standard Gibbs energy of formation of species $A_i^{(j)}$ and $K_j$ is the equilibrium constant of the $j$th reaction. Because molality $m$ is used in this work as the concentration unit, the equilibrium constant is expressed as

$$K_j = \prod_{i=1}^{n_j} \left(m_{A_i^{(j)}} \gamma_{A_i^{(j)}}\right)^{\nu_i^{(j)}}, \qquad (j = 1, \ldots, k). \tag{13}$$

where $\gamma_{A_i^{(j)}}$ is the activity coefficient of species $A_i^{(j)}$.

The chemical equilibrium equations (12) and (13) are solved simultaneously by using mass and electroneutrality balance equations. To solve this system of equations, the standard Gibbs energies of formation and activity coefficients are calculated as described before.

For example, let us consider a system obtained by mixing soluble salts of lead (e.g., lead acetate or lead nitrate) and titanium dioxide. Table 1 contains equilibrium equations for 42 aqueous and solid species that may exist in the Pb–Ti–$H_2O$ system. The presence of nitric acid and potassium hydroxide (see Table 1) results from the fact that the formation of ceramic materials (e.g., lead titanate) may require pH-adjusting agents such as acids, alkaline, hydroxides, or ammonia. For completeness, the data for gaseous species are also included, even though the gas phase plays a secondary role in perovskite synthesis under the $T$–$P$ conditions of interest. As we can see in Table 1, even a relatively simple hydrothermal system such as Pb–Ti–$H_2O$ contains a large number of species and a correspondingly large number of equations to be solved.

## Standard-State Properties

The standard Gibbs energy of formation at the temperature and pressure of interest is calculated from the standard Gibbs energy $\Delta G_f^\circ$, enthalpy $\Delta H_f^\circ$ of formation, and entropy $S^\circ$ at a reference temperature (usually 298.15 K) as well as partial molar volume $V^\circ$ and heat capacity $C_p^\circ$ as functions of temperature. The OLI data bank contains information for many aqueous, gaseous, and solid

**Table 5. Reaction Equilibria in the Pb–Ti Hydrothermal System Using $TiO_2$ and $PbAc_2$ and/or $Pb(NO_3)_2$ as Starting Materials**

| | |
|---|---|
| $H_2O = H^+ + OH^-$ | $PbAc_{2(aq)} = PbAc^+ + Ac^-$ |
| $H_2O_{(g)} = H_2O$ | $PbAc_3^{2-} = Pb^{2+} + 3Ac^-$ |
| $TiO_{2(s)} + OH^- = HTiO_3^-$ | $PbAc_{2(s)} = Pb^{2+} + 2Ac^-$ |
| $Ti^{4+} + H_2O = TiOH^{3+} + H^+$ | $PbNO_3^+ = Pb^{2+} + NO_3^-$ |
| $TiOH^{3+} + H_2O = Ti(OH)_2^{2+} + H^+$ | $Pb(NO_3)_{2(aq)} = PbNO_3^+ + NO_3^-$ |
| $Ti(OH)_2^{2+} + H_2O = Ti(OH)_3^+ + H^+$ | $Pb(NO_3)_{2(s)} = Pb^{2+} + 2NO_3^-$ |
| $Ti(OH)_3^+ + H_2O = Ti(OH)_{4(aq)} + H^+$ | $HAc_{(g)} = HAc_{(aq)}$ |
| $Ti(OH)_{4(aq)} + OH^- = HTiO_3^- + 2H_2O$ | $HAc_{(aq)} = H^+ + Ac^-$ |
| $TiO_2(rutile) + 2H_2O = Ti(OH)_{4(aq)}$ | $Ac_{2(aq)} = 2HAc_{(aq)}$ |
| $TiO_2(anatase) + 2H_2O = Ti(OH)_{4(aq)}$ | $Ac_{2(vap)} = Ac_{2(aq)}$ |
| $PbO(litharge) + H_2O = Pb^{2+} + 2OH^-$ | $HNO_{3(g)} = HNO_{3(aq)}$ |
| $PbO(massicot) + H_2O = Pb^{2+} + 2OH^-$ | $HNO_{3(aq)} = H^+ + NO_3^-$ |
| $PbO_{(aq)} + H_2O = PbOH^+ + OH^-$ | $KOH_{(s)} = K^+ + OH^-$ |
| $Pb(OH)_{2(s)} = Pb^{2+} + 2OH^-$ | $KOH \cdot H_2O = K^+ + OH^- + H_2O$ |
| $PbOH^+ = Pb^{2+} + OH^-$ | $KOH \cdot 2H_2O = K^+ + OH^- + 2H_2O$ |
| $Pb^{2+} + 2OH^- = HPbO_2^- + H^+$ | $KAc_{2(aq)} = K^+ + Ac^-$ |
| $Pb_2OH^{3+} + H^+ = 2Pb^{2+} + H_2O$ | $KNO_{3(s)} = K^+ + NO_3^-$ |
| $PbTiO_{3(s)} + 3H_2O = Pb^{2+} + 2OH^- + +Ti(OH)_{4(aq)}$ | $K_2TiO_{3(s)} + 3H_2O = 2K^+ + Ti(OH)_{4(aq)} + 2OH^-$ |
| $PbAc^+ = Pb^{2+} + Ac^-$ | |

compounds. Whenever possible, data should be taken from critically evaluated and consistent sources. These compilations were discussed previously along with criteria for selecting the most reliable data (29). Extensive work on the application of the HKFT equation (38,39) are a main source of data for aqueous species. Data for solid compounds are usually taken from the compilations of the NBS (40,41), JANAF (42), Medvedev et al. (43), and Robie et al. (44). For ceramic materials, especially double oxides (e.g., lead and alkaline-earth titanates), most of the data are available in the book by Barin (45).

Solubility data for solid compounds in pure water as well as in alkaline and/or acidic solutions at different temperatures are the best source of data for standard-state properties. These data are available in books by Seidell and Linke (46,47), and in the current literature. Whenever possible, regression of solubility data are performed using the OLI software (30) to obtain accurate and consistent thermochemical data for solid compounds.

In many cases, no experimental data are available for aqueous and solid species of interest, and predictive methods are necessary. If the HKFT equation parameters are not available from the regression of experimental data, they can be estimated. For this purpose, Shock and Helgeson (38,39) presented correlations for most solution species, except for complexes. Sverjensky (48) developed an estimation method for several classes of complexes. In addition to the HKFT equation parameters, these methods make it possible to predict the reference-state enthalpy and entropy if the reference-state Gibbs energy is known. These and other estimation techniques have been reviewed in detail by Rafal et al. (27).

At the same time, empirical procedures for calculating the standard-state properties of perovskite-type multicomponent (double) oxides of the general formula $ABO_3$ (A = Ca, Sr, Ba, Pb, etc.; B = Ti, Zr, etc.) have been developed (49) based on a family analysis (50,51) or group contribution methods (52). In our work, unavailable thermochemical properties for lead zirconate and lead, magnesium, and zinc niobates were estimated by using these methods.

No thermodynamic properties are available for solid solutions (e.g., PZT, PMN, PZN), and no experimental solubilities were measured. Therefore, estimation methods are necessary. They include calculations of thermochemical data based on the ideal solid solution approximation. A less sophisticated alternative is the use of group contribution methods. A more rigorous approach is based on analyzing the thermodynamic properties of solid solutions in terms of the thermodynamic functions of mixing. This approach was applied to calculate standard-state properties of PZT solid solutions (14).

Note that the number of potentially stable solid phases in some multicomponent systems can be very large. For example, in the Pb–Mg–Nb–K hydrothermal system, we are dealing with a large number of solid phases (i.e., oxides, hydroxides, niobates etc.). Therefore, in such a complicated system for which a great deal of estimation is necessary, we used the model interactively with experimentation to establish the solid phases that are likely to form. It may greatly suppress or increase the number of phases included in the model, whose properties can be estimated as mentioned earlier. Furthermore, experimentation can provide feedback for adjusting the magnitude of certain thermochemical data, whose origin may be questionable.

## STABILITY AND YIELD DIAGRAMS

The purpose of our work was to calculate the optimum synthetic conditions for forming phase-pure materials. This information can be obtained from knowledge of the stability and yield diagrams calculated for hydrothermal systems involving ceramic materials. In the past, stability diagrams were considered for a limited number of hydrothermal systems by assuming that the aqueous solutions were ideal (8,53).

Repetitive application of the model for different input concentrations of the A-site and B-site precursors as well as pH-adjusting agents (mineralizers) makes it possible to construct stability and yield diagrams. Stability diagrams show the ranges of equilibrium conditions for which various aqueous and/or solid species are stable in the hydrothermal system. Equilibrium conditions include the total molality of a selected aqueous metal precursor, solution pH, and temperature. The total molality of the aqueous metal precursor is the sum of the equilibrium concentrations of all dissolved metal species and does not include the species that precipitate from the solution as solids. The stability diagrams provide information about the conditions for incipient precipitation of various solid phases, but they do not specify the reaction conditions required for an assumed yield of a reaction product. The idea of yield diagrams was conceived to achieve this goal (12). In contrast to stability diagrams, the yield diagrams shown have the total input concentration of the metal precursor as the independent variable instead of the equilibrium (total) concentration of all dissolved metal species. The metal precursor can be converted to the desired product (e.g., $ABO_3$) that gives a certain yield, and the reminder of the metal precursor can remain in the solution. For the purpose of yield analysis, it is necessary to use the input concentration because we are concerned with the equilibrium concentration of species in saturated solution and also with converting the precursor system into a phase-pure product. Thus, the input concentration of the metal precursor takes into account all metal-containing solution and solid species. In our previous papers (11–14), yield diagrams were constructed point by point, whereas later, a computer program was developed to generate these diagrams automatically (15).

As the $y$-axis variable of yield diagrams, the program uses the input concentrations of one or more starting materials which is equal to the initial concentration of the metal precursor. To simplify the graphical output in multicomponent metal oxide systems, the ratios of the input precursor concentrations are held constant at a predetermined value. As the $y$-axis variable of stability diagrams, the program uses the total concentrations of one or more metal precursors. As the $x$-axis variable, the program can use either pH or the input concentration of a mineralizer. All concentrations are expressed in molalities because such units are easily measurable. Temperature can also be used as the $y$-axis variable, and all precursor concentrations can be used as $x$-axis or $y$-axis variables. If pH is chosen as the $x$-axis variable, the program changes the equilibrium pH by adding varying amounts of a selected acid (e.g., $HNO_3$) and a base (e.g., KOH). Note that the pH values are calculated at the temperature of an experiment at equilibrium. For example, pH values in alkaline solutions at 433–473 K are smaller by about 2–3 pH units than those for the same solutions at room temperature.

If the input concentration of a pH-adjusting agent is chosen as the $x$-axis variable, it is varied by the program on a linear or logarithmic scale. Note that the diagrams developed in previous papers (11–14,29) were always constructed so that the total or input concentration of the metal precursor, equilibrium pH, or temperature is the $y$-axis variable and equilibrium pH or temperature is the $x$-axis variable. The automatic generation of diagrams allows us to be more flexible in choosing of independent variables. This is particularly useful when it is necessary to determine the amount of a pH-adjusting agent that is needed to obtain a certain yield of the product.

The stability diagrams include two types of lines: the solid lines denote the states of incipient precipitation of solids, whereas the dotted lines show the loci where two aqueous species have equal concentrations. In practice, it is assumed that an equilibrium point lies on the solid to aqueous species boundary (solubility curve) when less than 0.25% of the precursor is found as a solid phase. The yield diagrams show the areas where the desired product precipitates in a yield greater than or equal to an assumed value (e.g., 99%). At the solubility curve (shown in both stability and yield diagrams), the yield is very small because the solubility curve corresponds to incipient precipitation of the desired product. The yield increases as we move beyond the solubility curve into the solid–liquid region. This yield is calculated by dividing the number of moles of the product by the total number of moles of the input metal precursor. The yield areas are shown in the diagrams as shaded fields. Usually, the boundaries between aqueous species are not shown in the yield diagrams. Note that yield diagrams provide direct guidance for experimental synthesis because the shaded area of the yield diagram shows the range of input precursor concentrations that can produce a phase-pure product.

A certain ratio of metals in the starting materials (i.e., A/B) is assumed by choosing the precursor system for hydrothermal synthesis. It may correspond to the stoichiometric ratio in the formula of the perovskite (i.e., $ABO_3$) or can be greater or lower than one. If the ratio is lower than one, the formation of the perovskite phase does not go to completion. If it is greater than one, the perovskite and possibly additional phases containing A-site metals form. If the ratio is equal to one, we may expect the formation of phase-pure $ABO_3$ if thermodynamics drives the following reaction to completion (i.e., reaction (14) has a large equilibrium constant):

$$A^{2+} + BO_2 + 2OH^- = ABO_3 + H_2O \qquad (14)$$

Thus, to make phase-pure $ABO_3$, reaction conditions where the ratio A/B equals or exceeds one are the most useful to optimize. In the section that follows, we present examples where we have achieved this.

### Stability and Yield Diagrams for the Stoichiometric Ratio of Precursors $A/B = 1$

Figure 1 shows the stability diagram calculated for the hydrothermal system obtained by mixing lead nitrate or lead acetate and titanium dioxide at $T = 433$ K. The stoichiometric molar ratio Pb/Ti = 1 is employed. The total molality of all lead species in the solution and the solution pH are used as independent variables. The solid curved line on the stability diagram corresponds to the states of incipient precipitation of $PbTiO_3$. On the other hand, the vertical straight lines correspond to the loci where two aqueous species have equal concentrations. As shown in Fig. 1, the chemical identity of these species varies with pH.

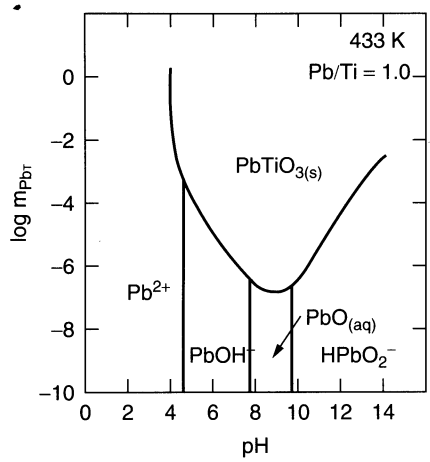


**Figure 1.** Calculated stability diagram for the Pb–Ti system at 433 K. $PbAc_2$ and $TiO_2$ are used as starting materials, and the ratio of total molalities is 1.0.

$Pb^{2+}$ dominates at pH below 4.3, but it becomes hydrolyzed to $PbOH^+$ at 4.3 < pH < 7.8. Further, the neutral species $PbO_{(aq)}$ becomes predominant at 7.8 < pH < 9.2 and is, in turn, replaced by $HPbO_2^-$ above pH 9.2. The formation of the desired product, $PbTiO_3$, is depends strongly on pH. Crystalline $PbTiO_3$ can be obtained at a pH higher than ca. 4.0. The stability of $PbTiO_3$ increases as pH rises and reaches a maximum at pH 8.5. In this pH range, $PbTiO_3$ precipitates when the concentration of lead in solution is as low as $10^{-7}$ *m*. The stability of $PbTiO_3$ decreases somewhat above pH 10 because of the amphoteric character of lead. Thus, the solubility curve of $PbTiO_3$ is parabola. The incipient precipitation line of $PbTiO_3$ is practically insensitive to the chemical identity of lead precursors. A very small shift in pH (about 0.2 units) is caused by the existence of various lead nitrate and lead acetate complexes in this system (see Table 1).

Figure 2 shows the comparison of the conditions for synthesizing the alkaline-earth titanates, $CaTiO_3$, $SrTiO_3$, and $BaTiO_3$. It combines the calculated phase stability diagrams for three hydrothermal systems Ca–Ti, Sr–Ti, and Ba–Ti at 433 K. The diagrams are qualitatively similar because of the chemical similarity of Ca, Sr, and Ba cations. The total molality of the alkaline-earth metal precursor and the pH of the solution adjusted by KOH are chosen as independent variables. Three incipient precipitation lines are shown in this figure. The lines for the beginning of precipitation of $CaTiO_3$ and $SrTiO_3$ are very close to each other. The $BaTiO_3$ line is located at a somewhat higher pH. Its distance from the $SrTiO_3$ line is about 1.2 pH units. The relative location of the incipient precipitation lines results from an interplay of several independent factors. Among them, most important are the relative magnitude of standard-state thermodynamic functions, the alkalinity of the Ba, Sr, and Ca species as well as specific interactions between ions that determine the activity coefficients. It is apparent that the incipient precipitation line for the titanate of the most alkaline metal, i.e., Ba, lies at higher pH values. The differences between the $CaTiO_3$ and $SrTiO_3$ lines become visible only at relatively high and small (but not intermediate) concentrations. The $CaTiO_3$ and $SrTiO_3$ lines cross each other. If the input concentration of titanium dioxide is 0.1 *m*, barium titanate precipitates above pH 8, strontium titanate begins to form above pH 7.5, and calcium titanate occurs at above pH 7.3 at 433 K. The predominant areas of alkaline-earth cations and their hydroxy complexes are also shown in this figure.

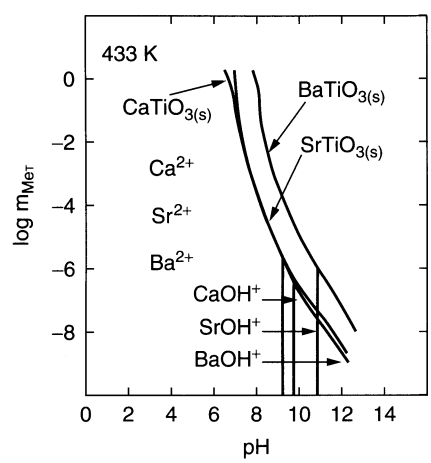


**Figure 2.** Comparison of calculated phase stability diagrams for the hydrothermal systems Ca–Ti, Sr–Ti, and Ba–Ti at 433 K for the stoichiometric molar ratios of precursors.

Figure 3 shows a yield diagram for the Pb–Zr–Ti hydrothermal system calculated at 433 K (14). Lead acetate and zirconium and titanium dioxide at a molar ratio of 0.52/0.48 were used as precursors. KOH was used to adjust pH and the Pb/(Zr+Ti) ratio was one. The area of stability of a solid solution $PbZr_{0.52}Ti_{0.48}O_3$ (PZT) is encompassed

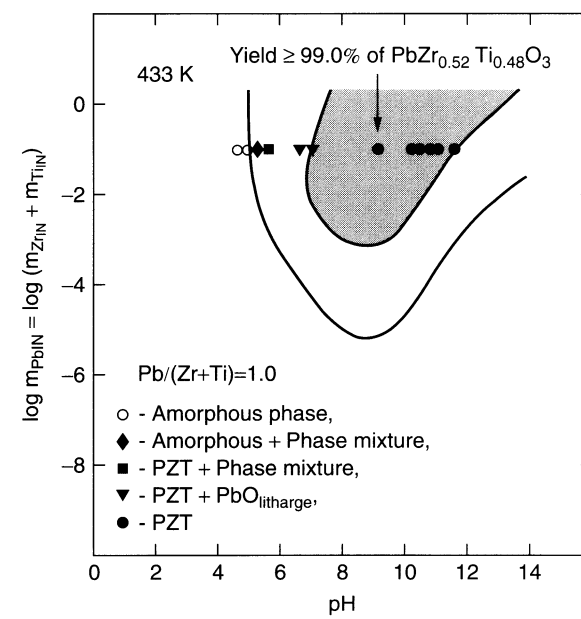


**Figure 3.** Calculated yield diagram of $PbZr_{0.52}Ti_{0.48}O_3$ at 433 K. $PbAc_2$, $TiO_2$, and $ZrO_2$ are used as starting materials for the calculations. Symbols denote various solid phases that were experimentally obtained using $PbAc_2$ and coprecipitated Zr–Ti hydrous oxides, $Zr_xTi_{1-x}O_2 \cdot nH_2O$.

by a parabolic solid line. The exact pH value at which precipitation begins depends on the total concentration of Pb in the aqueous phase. For example, if the concentration of lead precursor is 0.1 *m*, the precipitation of the solid solution starts above pH 4.9. If lead nitrate is used, the left boundaries are shifted toward lower pH values by about 0.3–0.4 pH units, whereas the right boundaries remain the same. The area of PZT solid solution stability increases at higher concentrations. For relatively concentrated solutions, dissolution of solid PZT phases occurs above pH 14.0. The effect of temperature on the diagram is minimal in the range from ca. 433 to 573 K. At 573 K, the incipient precipitation lines shift toward lower pH values by about 0.2–0.4 units. The area of PZT yield greater than 99.0% is much smaller than the stability region. It is illustrated in Figure 3 as a shaded region encompassed by a solid line. For the input concentration of lead and, subsequently, the sum of the input concentrations of Ti and Zr, equal to 0.1 *m*, phase-pure PZT forms above pH 6.8 and below 11.4. Because the yield diagrams are somewhat sensitive to the chemical identity of precursors (12), calculations were performed using lead nitrate as a precursor. In this case, the area of PZT yield greater than 99% is shifted toward lower pH values by about 0.8–0.9 pH units.

One of the possible ways of presenting yield diagrams is calculating stability and yield of ceramic materials at different temperatures as a function of the solution pH. Figure 4 summarizes theoretical findings for the synthesis of $PbTiO_3$ from lead acetate and/or lead nitrate and titanium dioxide for the Pb/Ti ratio of one. Figure 4 is valid for

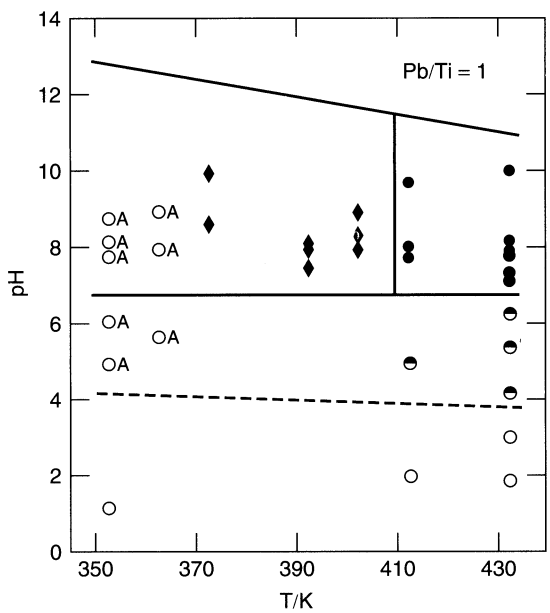


**Figure 4.** Solid products of hydrothermal reactions of $PbAc_2$ and/or $Pb(NO_3)_2$ and $TiO_2$ for the input molality of lead of 0.05–0.2 *m* at different temperatures and pH values: solid circles—crystalline $PbTiO_3$, A—amorphous $PbTiO_3$, hollow circles—$TiO_2$, semi-solid circles—$PbTiO_3 + TiO_2$, solid diamonds—$PbTiO_3 + TiO_2 + PbO$ (massicot) + $Pb_2Ti_2O_6$. The dashed line denotes the beginning of $PbTiO_3$ precipitation, and the solid lines encompass the region where the yield of $PbTiO_3$ exceeds 99.99%.

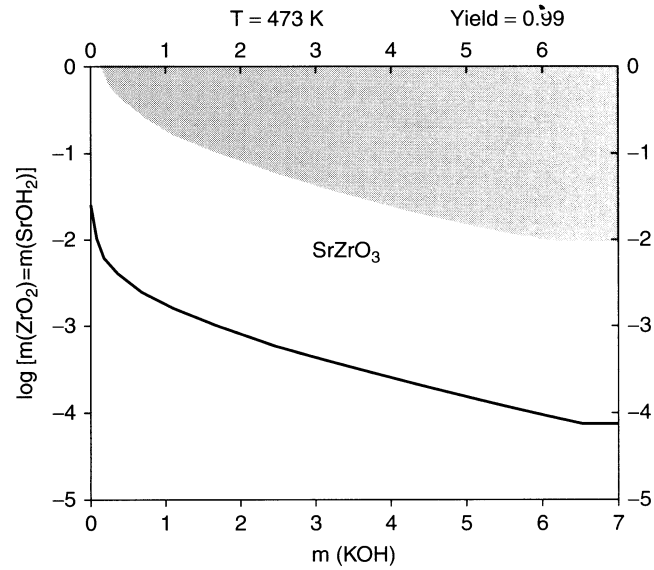


**Figure 5.** Calculated phase stability and yield diagram as a function of the input amount of KOH at 473 K for Sr/Zr = 1 using $Sr(OH)_2$ as a source of strontium.

input reagent concentrations ranging from 0.05 to 0.2 *m*, which are convenient for carrying out the reactions in practice. The dashed line corresponds to the beginning of the precipitation of lead titanate. The solid lines encompass the region of yield greater than 99.99% $PbTiO_3$, which is appropriate for practical syntheses. The areas between the dashed and lower solid lines and upper solid line and pH 14 correspond to the precipitation of $PbTiO_3$ along with unreacted solid titanium dioxide. The region between the pH 0 axis and the dashed line shows the conditions for which the synthetic reaction does not occur. In this region, unreacted solid titanium precursor and aqueous species coexist. For clarity, aqueous lines are not shown in the yield diagrams.

The stability and yield diagrams where pH is an independent variable (Figs. 1–4) do not indicate the concentration of a pH-adjusting agent necessary to synthesize the desired product. Figure 5 shows the calculated phase stability and yield of strontium zirconate obtained by mixing strontium hydroxide and zirconium oxide at 473 K. In this figure, the Sr and Zr precursors, at a fixed molar ratio (Sr/Zr = 1), are used as *y*-axis variables, and pH is replaced by the molality of a base (KOH) as an *x*-axis variable. The solid line in Fig. 5 denotes the beginning of the precipitation of strontium zirconate. Strontium zirconate and zirconium oxide coexist in the area above the solid line. As we move closer to the shaded area, the yield of strontium zirconate increases, and the amount of zirconium dioxide decreases. The shaded region shows the optimum synthetic conditions (i.e., input molality of strontium hydroxide and potassium hydroxide) to form phase-pure strontium zirconate (yield greater than 99%) at 473 K. The amount of KOH necessary to form phase-pure $SrZrO_3$ from $Sr(OH)_2$ is much smaller than that from strontium nitrate (15) but cannot be completely eliminated (see Fig. 5). The minimum amount of KOH is as low as 0.2 *m* when the input concentration of $Sr(OH)_2$ is 1 *m* but rises to 1.6 *m* for an input concentration of 0.1 *m*.

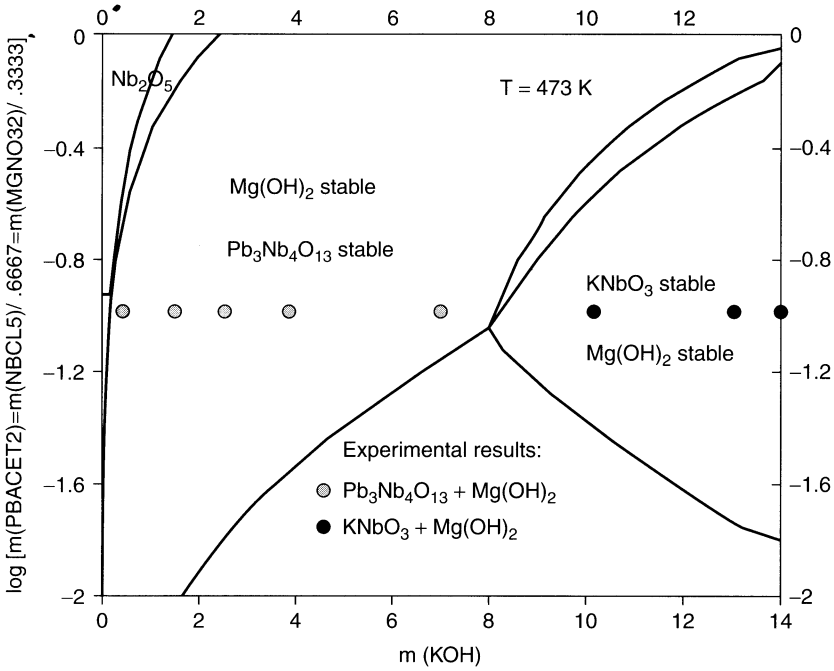


**Figure 6.** Stability of various solid phases in the Pb–Mg–Nb–K–$H_2O$ system at 473 K.

All of the previous diagrams showed that it is possible to synthesize phase-pure titanates and zirconates if the synthetic conditions are carefully chosen. Compositions in the perovskite family whose the general formula is $Pb(B_1,B_2)O_3$ are known as ferroelectric relaxors and are of considerable interest. It has been reported in the literature (54) that these materials are difficult to fabricate reproducibly without the appearance of a pyrochlore phase that can be detrimental to the dielectric properties. Lead magnesium niobate [$Pb(Mg_{1/3}Nb_{2/3})O_3$ or PMN] attracted our attention because it has never been obtained hydrothermally at moderate temperatures. An analysis of the stability of perovskite materials in vacuum based on quasi-thermodynamics and crystal chemical arguments by Shrout and Halliyal (55) showed that the problem of pyrochlore formation in the preparation of PZN and PMN is primarily thermodynamic. Therefore, it was of interest to study whether the high stability of pyrochlores (such as $Pb_{1.83}Mg_{0.29}Nb_{1.71}O_{6.39}$ or $Pb_3Nb_4O_{13}$) in the Pb–Mg–Nb–$H_2O$ system is also responsible for the failure to obtain phase-pure tetragonal PMN hydrothermally. One of the main steps in calculating the stability of the phase of interest (PMN) is to find or estimate thermochemical data for solid phases that are likely to form under hydrothermal conditions. Note that the number of potentially stable solid phases in this system is very large and consists of oxides and hydroxides of lead, magnesium and niobium; various niobates of magnesium, lead, and potassium; and solid solutions; which include a tetragonal and a cubic PMN pyrochlore phase and possibly a solid solution between potassium niobate and lead magnesium niobate.

Our original data bank did not contain thermochemical properties of most of these solids, except for magnesium and lead oxides and hydroxides. Therefore, thermochemical data for $Nb_2O_5$, $Pb(NbO_3)_2$, and $KNbO_3$ were calculated from the reported solubilities of these species in aqueous solutions (31,46–47). The thermochemical properties of multicomponent oxides (niobates) were calculated by using a group contribution method (30,51). Then, based on the new values for the end members, thermochemical properties of the solid solutions were calculated by using an ideal solid solution approximation. Figure 6 shows the calculated stability of various solid phases in the Pb–Mg–Nb–K–$H_2O$ system at 473 K. The input molality of lead, magnesium, and niobium precursors at a ratio corresponding to the stoichiometry of tetragonal PMN is shown on the $y$ axis, and the KOH concentration is shown on the $x$ axis. The solid lines encompass the regions where various solid materials are stable. For example, $Nb_2O_5$ is stable in an acidic environment at low amounts of KOH and at a relatively high concentration of niobium in the solution. Lead niobate ($Pb_3Nb_4O_{13}$) is extremely stable and starts to precipitate at very low concentrations of KOH. At high concentrations of KOH, lead niobate dissolves to release Nb ions into the solution to form potassium niobate ($KNbO_3$). The stability regions of $Mg(OH)_2$ and the $Pb_3Nb_4O_{13}$ pyrochlore phase overlap at low pH values, but magnesium hydroxide is very stable in highly alkaline solutions and overlaps $KNbO_3$ in this region. These calculations are summarized in Fig. 6, which shows that tetragonal PMN is not thermodynamically stable because magnesium hydroxide and lead niobate are more stable than tetragonal PMN in basic aqueous solutions. Furthermore, the use of KOH mineralizer causes the formation of $KNbO_3$. Organic mineralizers such as tetramethylammonium hydroxide ($Me_4NOH$) do not form niobates, but they still cause the formation of $Pb_3Nb_4O_{13}$ and $Mg(OH)_2$, instead of tetragonal PMN (31). Note that standard-state properties for many solid compounds in this system were estimated. Therefore, this is a preliminary phase and stability diagram of the Pb–Mg–Nb–K hydrothermal system, which may be fine-tuned in the future.

### Stability and Yield Diagrams for the Nonstoichiometric Ratio of Precursors (A/B > 1)

When the A/B ratio is higher than one, we expect that the area of phase-pure product in the yield diagrams will increase because an excess of A-site metal in solution shifts the equilibrium, so that a pure perovskite phase precipitates at lower pH values, which also reduces the amount of mineralizer required. However, an excess of metal A can also cause the precipitation of secondary phases. In lead-containing hydrothermal systems, an excess of lead forms lead hydroxide or lead oxide (litharge) (12). Hydrated and nonhydrated forms of hydroxides can precipitate together with the desired ceramic material in systems that contain an alkaline-earth metal (13,15,29). Some of these impurities can be eliminated by washing, but leaching of A-site ions from the perovskite lattice is also an important concern (56). Thus, an excess of A metal is useful provided that syntheses are performed in the pH region where additional solid phases do not precipitate.

Figure 7 shows a yield diagram in the Pb–Ti–$H_2O$ system constructed using lead acetate and titanium oxide at a Pb/Ti ratio of 1.5. This figure shows the pH–$T$ regions where different solid phases can be obtained for an input concentration of lead precursor of 0.1 $m$. The dashed line represents the beginning of the precipitation of $PbTiO_3$, The region between the axis pH 0 and the dashed line shows conditions where the reaction does not occur. In the area between the dashed and solid lines, $PbTiO_3$ precipitates along with unreacted $TiO_2$. In Fig. 7, the dot-dashed line shows the beginning of PbO (litharge) precipitation. Phase-pure perovskite precipitates between the solid and dot-dashed lines. Thus, the area above the dot-dashed line corresponds to the region where phase-pure $PbTiO_3$ cannot be obtained because of the presence of an additional solid phase, PbO. A comparison of Figs. 4 and 7 shows that an excess of Pb decreases the pH for the formation of phase-pure $PbTiO_3$ by about 2 pH units. Consequently, less mineralizer is neccesary to obtain a pure phase. However, the region of phase purity is relatively small and limited to 1 pH unit. At higher alkalinities, lead oxide precipitates along with lead titanate. The extent of the phase-purity region depends strongly on the Pb/Ti ratio (12,57,58).

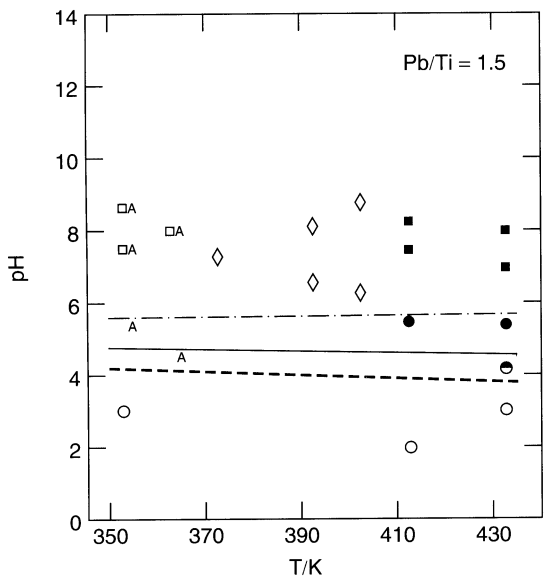


**Figure 7.** Solid products of hydrothermal reactions of $PbAc_2$ and $TiO_2$ for an input concentration of lead 0.1 $m$ at different temperatures and pH values: solid circles - crystalline $PbTiO_3$, A - amorphous $PbTiO_3$, hollow circles - $TiO_2$, semi-solid circles - $PbTiO_3 + TiO_2$, open diamonds - PbO (litharge and massicot) + $Pb_2Ti_2O_6 + TiO_2$, hollow squares - PbO (litharge and massicot), and solid squares - $PbTiO_3$ + PbO (litharge and massicot). The dashed line denotes the beginning of $PbTiO_3$ precipitation, the solid and dot-dashed lines encompass the region where the yield of $PbTiO_3$ exceeds 99.99%, and the dot-dashed line denotes the beginning of PbO precipitation.

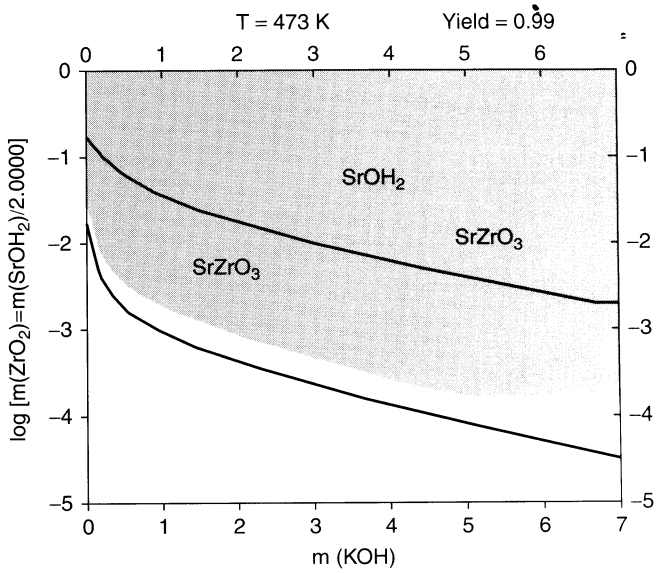


**Figure 8.** Calculated phase stability and yield diagram as a function of the input amount of KOH at 473 K for Sr/Zr = 2.0 using $Sr(OH)_2$ as a source of strontium. The solid circle denotes experimental conditions for which phase-pure $SrZrO_3$ was obtained.

Figure 8 shows the calculated phase stability and yield diagram as a function of the input molality of KOH at 473 K for a Sr/Zr ratio of 2.0 in the Sr–Zr hydrothermal system. Strontium hydroxide and zirconium dioxide were used as precursors. In comparison with the Sr/Ti ratio of 1.0 (see Fig. 5), the beginning of $SrZrO_3$ precipitation shifts very slightly toward lower concentrations of the input metal precursors, thus suggesting that a slightly lower pH is necessary to form pure strontium zirconate. The region of nearly complete yield of $SrZrO_3$ (>99%) is much greater than for Sr/Zr = 1.0 and starts at lower amounts of KOH (see Fig. 5) and correspondingly lower pH values (15). No mineralizer is necessary when the input concentration of Zr exceeds 0.02 $m$. The upper solid line in Fig. 8 represents the incipient precipitation line of strontium hydroxide. In the area above this line, $SrZrO_3$ is always contaminated by $Sr(OH)_2$.

Our work has also examined the possibility of using organic mineralizers (58). The next diagram shows the calculated yield of lead zirconate titanate ($PbZr_{0.6}Ti_{0.4}O_3$) at 433 K at the ratio of lead acetate to the sum of titanium and zirconium dioxide of 1.1. In Fig. 9, the input modalities of Ti precursor are plotted against the molality of

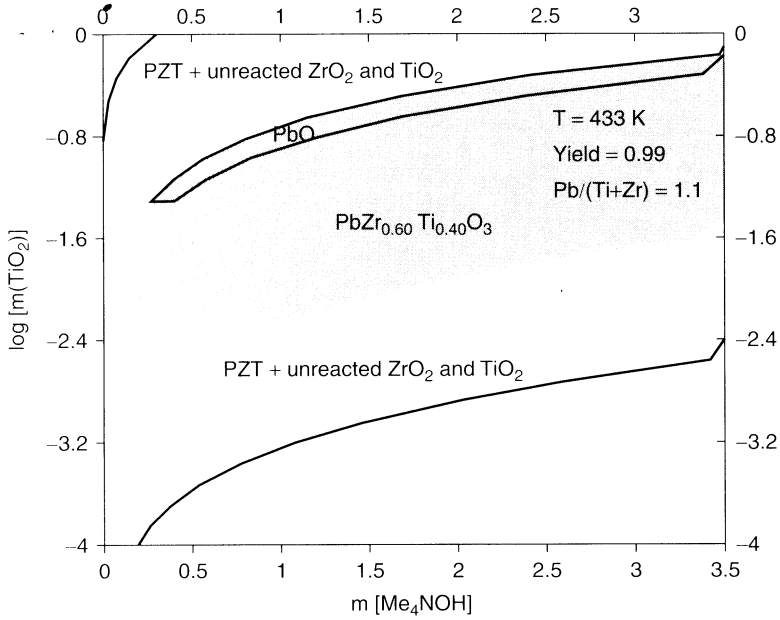


**Figure 9.** Calculated yield diagram of $PbZr_{0.6}Ti_{0.4}O_3$ at 433 K. $PbAc_2$, $TiO_2$, and $ZrO_2$ are used as starting materials for the calculations.

tetramethylammonium hydroxide ($Me_4NOH$). The upper left and lower solid lines encompass the region of rhombohedral PZT stability. They belong to the incipient precipitation line. Phase-pure $PbZr_{0.6}Ti_{0.4}O_3$ can form in a relatively wide region of input precursor and mineralizer molalities (see shaded area in Fig. 9). $PbZr_{0.6}Ti_{0.4}O_3$ precipitates along with PbO in the small region shown at the top of the phase-purity region. The stability area of PbO is relatively small and limited to high concentration of precursors. Lead oxide dissolves in highly alkaline solutions. When the ratio of metals in precursor materials is greater than one, the area of the perovskite phase-purity region widens. However, under some reaction conditions, it causes contamination of ceramic materials by additional phases.

### Carbon Dioxide Contamination

There are three general ways to introduce $CO_2$ into a hydrothermal product:

1. contaminated starting materials (e.g., alkaline and alkaline-earth hydroxides, hydrous oxides),
2. synthesis unit operation in a high pH precursor solution (the absorption of $CO_2$),
3. postsynthesis unit operations (i.e., during washing, filtration, etc.).

To eliminate the risk of carbonate contamination by starting materials, all reagents should be free from carbonates. However, carbonate-free alkaline-metal hydroxides (i.e., precursors) and alkaline hydroxides (i.e., mineralizers) are not available commercially. For example, according to the manufacturer (Aldrich), the 99.99% (adjusted to cation) electronic grade KOH contains 0.4 wt% of $K_2CO_3$. On the other hand, commercially available alkaline-earth hydroxides usually contain 0.5–3 wt% $CO_2$. The weight percent of alkaline-earth carbonate in the final product can be calculated by assuming that all $K_2CO_3$ contained in KOH converts to $ACO_3$ (A = Ba, Sr, Ca). In principle, carbonates can be removed from the final product by washing using a weak acid, but the risk of dissolving ceramic materials in acids is very high, as suggested in the stability and yield diagrams (see Figs. 1–10). Therefore, it is advisable to purify commercial hydroxides and or hydrates by filtering metal carbonate contaminants from a hot stock solution of the corresponding hydroxide or and hydrate.

The problem of contaminating the solution by carbonates during preparation of starting materials has been discussed in our previous papers (11,13). Unless the system is isolated from the atmosphere, contact with $CO_2$ may occur during the preparation of precursor solutions. The effect of atmospheric $CO_2$ on the purity of alkaline-earth titanates and zirconates is different for Ca-, Sr- and Ba-containing hydrothermal systems. It is directly correlated with the alkalinities of Ca, Sr, and Ba because the absorption of $CO_2$ is facilitated by the alkalinity of the solution. Accordingly, the metal concentration thresholds above which carbonates precipitate are different for the three systems. For example, the contact of alkaline strontium precursors with an open $CO_2$-containing air atmosphere will lead to contamination by $SrCO_3$ when the input concentration of Sr is higher than about $10^{-4}$ $m$ (11,15). Thus, it is beneficial to avoid contact with the atmosphere during the preparation of reagents. This is also the case when alkaline-earth metal salts (e.g., nitrates or acetates) are used as precursors in conjunction with NaOH or KOH as mineralizers because the presence of the mineralizers makes the solutions alkaline. However, our practical observations show that the absorption of atmospheric $CO_2$ may require a substantial amount of time which could be much longer than that required for experimental manipulations.

Washing and vacuum filtering of the synthesized products in air may cause additional contamination, especially when an excess amount of the A-site cation is present in alkaline environments. However, our study (15) shows

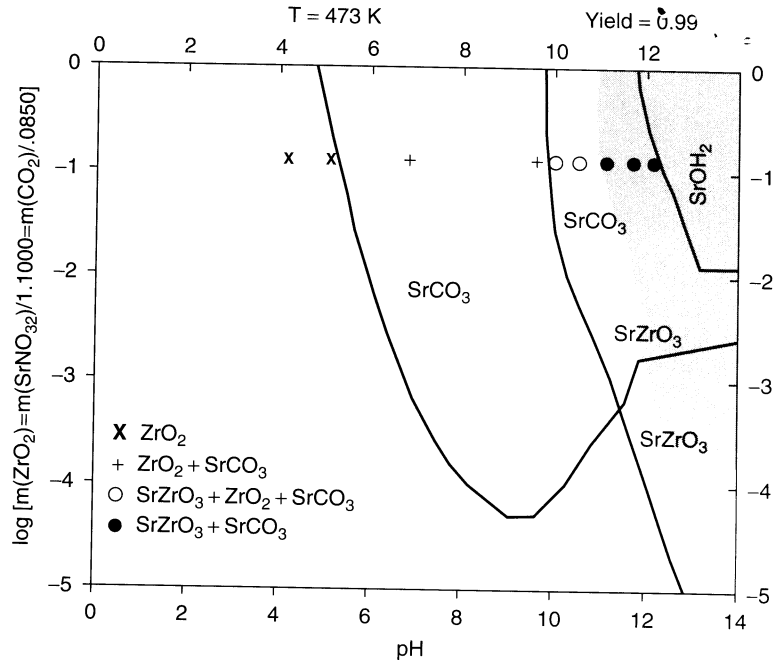


**Figure 10.** Calculated phase stability and yield diagram at 473 K for Sr/Zr = 1.1 using $Sr(NO_3)_2$ as a source of strontium when the amount of $CO_2$ in the starting materials is 0.085 times the amount of $ZrO_2$. The symbols denote experimental conditions for which the following products were obtained: **x**—$ZrO_2$, + – $SrCO_3 + ZrO_2$, ○—$SrZrO_3 + ZrO_2 + SrCO_3$, •—$SrZrO_3 + SrCO_3$.

that the existing carbonate content of the starting materials is the major determinant of product purity.

For our thermodynamic simulations, we assume that the carbonate contamination results primarily from the $CO_2$ content of starting materials. We have constructed stability diagrams for the Sr–Zr–$CO_2$–$H_2O$ system in which the amount of $CO_2$ is varied proportionally to the amount of the Sr and Zr precursors (15). This simulates a real-world situation in which $CO_2$ is a fixed fraction of a reactant. Figure 10 shows the effect of $CO_2$ on the stability and yield diagram plotted against the pH when the input amount of $CO_2$ is 0.085 times the amount of $ZrO_2$. This amount corresponds to the average concentration of carbon dioxide typically found in hydrous $ZrO_2$ and KOH in our reactions (15). In Fig. 10, the stability region of strontium carbonate is parabolic. Despite the small $CO_2$ content of the system, $SrCO_3$ is very stable, and its stability range almost overlaps the nearly complete yield range of strontium zirconate denoted by the shaded area. Strontium hydroxide is stable at very high pH, and its stability region overlaps those of strontium zirconate and strontium carbonate. Thus, it is predicted that $SrZrO_3$ is carbonate-free only in dilute solutions at high pH.

The hydrothermal equilibrium systems discussed in this article are representative examples of what can be achieved using our methodology. These examples show that for a given precursor system, thermodynamic calculations can be used to specify the optimum synthetic conditions to form phase-pure, smart perovskites. However, electrolyte thermodynamics computations alone are not sufficient. Sluggish reaction kinetics at low temperatures as well as the limited availability of thermochemical data for some species in the hydrothermal system can render conclusions derived from computations questionable. Therefore, experimental validation of the thermodynamic predictions is necessary.

## VALIDATION AND APPLICATIONS OF THERMODYNAMIC MODELING

To validate theoretical predictions, experiments are performed using the calculated stability and yield diagrams as a guide. In particular, hydrothermal syntheses are carried out at various metal precursor concentrations and ratios (A/B) for a wide pH range (mineralizer concentration) at each temperature. Thus, hydrothermal reactions are performed to investigate whether the locations of the various stability and yield regions agree with experimental findings. Soluble salts of lead and alkaline-earth metals are used as sources of the A-site cation in the hydrothermal synthesis. Such starting materials are inexpensive and easy to handle. Alkaline-earth metal hydroxides can also be used for this purpose (11,13,15). However, they usually contain carbonates (15) and, therefore, should be purified before use. Their low solubilities are also of concern (15). Commercial anhydrous or freshly precipitated hydrous oxides are used as a convenient source of the B-site cation; the latter are considered more reactive (12,14,15). From a practical point of view, a starting material concentration above 0.02 *m* is recommended. Reaction products are identified using X-ray diffraction. To verify phase purity further, other techniques such as wet chemical methods, thermogravimetric analysis, electron diffraction, energy dispersive spectroscopy, and other methods are employed. These tools are important if X-ray diffraction patterns are inconclusive. Experimental points are plotted in the corresponding regions of the yield diagrams (see Figs. 4, 7, 10).

Our simulation approach has been validated for numerous perovskite systems, including $BaTiO_3$ (59), $CaTiO_3$ (13), $SrTiO_3$ (11), $SrZrO_3$ (15), $PbTiO_3$ (12,57,58), various solid solutions of PZT (14,60), PMN (31), and PZN (31). The results indicate very good agreement between theoretical

predictions and experimental results for all systems investigated.

It is noteworthy that in some cases this agreement occurs only above a certain temperature that is characteristic for a precursor system (see Figs. 4 and 7) or in certain regions of the stability and yield diagrams (e.g., in the phase-pure region or at high pH; see Fig. 3). For example, there is excellent agreement between predictions and experiments at temperatures above 410 K in the Pb–Ti–$H_2O$ system (12) (see Fig. 4). However, the same agreement can be reached even at lower temperatures (above 363 K) in the same system by using complexing agents (57). The discrepancies at lower temperatures may be caused by sluggish reaction kinetics that can lead to the formation of metastable crystalline or amorphous products (see Figs. 4 and 7), which cannot be inferred from thermodynamic computations. The lack of thermodynamic data (e.g., for $Pb_2Ti_2O_6$ or amorphous precursors) and/or inaccurate data may also contribute to the disagreement.

Possible sources of disagreement may also result from the fact that the complexity of the thermodynamic system depends on the scale of mixing of all reagents. Note that thermodynamic calculations assume that all reagents are mixed on a microscopic scale. This is especially important for solid solutions. In practice, the mixture may not be homogenous. Thus, instead of a phase-pure product, phase separation results (14) such as precipitation of the end members of the solid solution system (e.g., PT and PZ instead of PZT) or formation of multiple phases [e.g., $CaTiO_3$ and $Ca(OH)_2$], which are likely far from equilibrium (12,14).

To validate the thermodynamic predictions move accurately, a special option called "an expert system" has been developed as a part of the OLI program. It makes it possible to design experiments that test the position of the yield boundary (see the shaded areas in Figs. 3–10). For this purpose, the expected yield and amount of ceramic material as well as the number of tests inside and outside the yield boundary are specified by the user in conjunction with the allowed variation in temperature and precursor concentration. As a result, the recommended metal precursor and mineralizer concentrations at each temperature are calculated.

Our computations for numerous systems have uncovered a series of thermodynamic trends. The systems investigated so far belong to two categories: alkaline-earth metal and lead-containing perovskites. Stability diagrams for alkaline-earth titanates ($CaTiO_3$, $SrTiO_3$ and $BaTiO_3$) are qualitatively similar because of the chemical similarity of Ca, Sr, and Ba cations. Their stability and yield regions are limited by lower boundaries with respect to pH (11,13) (see Figs. 2 and 10). In other words, alkaline-earth titanates and zirconates are stable in alkaline solutions and dissolve in acids or/and $CO_2$-containing water. The formation of phase-pure alkaline-earth titanates from metal hydroxides instead of metal nitrates or acetates at high input metal concentrations (higher than 0.1 *m*) does not require adding a mineralizer because the necessary concentration of $OH^-$ groups is readily provided by the hydroxide precursor (13). The presence of excess A-site ions in precursor reagents (i.e., A/B > 1) expands the width of the yield region closer to the incipient precipitation line. Thus, phase-pure products can form in less alkaline solutions, which is very important from economic and environmental points of view. However, if the pH becomes too high, alkaline-earth hydroxides precipitate as an impurity phase (see Fig. 10). Alkaline-earth metal–Ti–Zr–$H_2O$ systems also proved very vulnerable to contamination by carbonates (11,13,15) (see Fig. 10).

In contrast to alkaline-earth metals, lead is amphoteric. Its hydroxy complexes are relatively stable in highly alkaline environments. Therefore, the stability areas of PT, PZ, and PZT are parabolic (see Figs. 1, 3, 10). In other words, the stabilities of lead-containing perovskites are bounded by lower and upper pH limits. Although the presence of excess lead widens the yield region, it can also cause the precipitation of an unwanted PbO phase in the middle of the yield region (12). However, this problem has been solved by using complexing agents and our simulation-based approach (57). In contrast to alkaline-earth perovskites, carbonate contamination is not an issue in Pb–Ti–Zr–$H_2O$ systems because lead-containing carbonates [$2PbO{\cdot}PbCO_3$, $PbO{\cdot}PbCO_3$, $PbCO_3$, $2PbCO_3{\cdot}Pb(OH)_2$, and $PbCO_3$] are less stable than corresponding perovskites.

## CONCLUSIONS

A thermodynamic model of heterogeneous aqueous electrolyte systems, coupled with a facility for automatically generating stability and yield diagrams, provides a powerful tool for predicting the effect of various process conditions on the synthesis of smart ceramic materials. In particular, it makes it possible to determine the optimum conditions (*T*, pH, input precursor concentrations and ratios) for synthesizing various perovskite-type materials from simple precursors. The model is particularly valuable for analyzing the effects of changing the chemical identity and relative amounts of starting materials as well as for predicting the possibility of contamination by carbonates. The theoretical predictions allow us to formulate synthetic guidelines. To validate the results of theoretical predictions, experimental syntheses are performed in the whole temperature and pH range and for various input amounts of starting materials. Experience has demonstrated that this first-principles approach provides a very successful means for finding optimum synthetic conditions for forming perovskite-type multicomponent oxides.

## BIBLIOGRAPHY

1. Process for Producing Insoluble Titanates, US Pat. 2,216,655, Oct. 22, 1940, J.H. Peterson.
2. A.N. Christensen and S.E. Rasmussen, *Acta Chem. Scand.* **17**(3): 845 (1963).
3. A.N. Christensen, *Acta Chem. Scand.* **24**: 2447–2452 (1970).
4. T.R.N. Kutty, R. Vivekanandan, and P. Murugaraj, *Mater. Chem. Phys.* **19**: 533–546 (1988).
5. T.R.N. Kutty and R. Balachandran, *Mater. Res. Bull.* **19**: 1479–1488 (1984).
6. Process for Producing Submicron Ceramic Powders of Perovskite Compounds with Controlled Stoichiometry and

Particle Size, U.S. Pat. 5, 112, 433, May 12, 1992, W.J. Dawson and S.L. Swartz.

7. K.C. Beal, in *Advances in Ceramics*, Vol. 21, *Ceramic Powder Science*, G.L. Messing, K.S. Mazdiyasni, J.W. McCauley, and R.A. Haber, eds., American Ceramic Society, Westerville, OH, 1987, p.33.
8. D.J. Watson, C.A. Randall, R.E. Newnham, and J.H. Adair, in *Ceramic Transactions*, Vol. 1, *Ceramic Powder Science* IIA, G.L. Messing, K.S. Mazdiyasni, J.W. McCauley, and R.A. Haber, eds., American Ceramic Society, Westerville, OH, 1988, p. 154.
9. S. Kaneko and F. Imoto, *Bull. Chem. Soc. Jpn.* **51**(6): 1739–1742 (1978).
10. S. Komarneni, Q. Li, K.M. Stefansson, and R. Roy, *J. Mater. Res.* **8**(12): 3176–3183 (1993).
11. M.M. Lencka and R.E. Riman, *Ferroelectrics* **151**: 159–164 (1994).
12. M.M. Lencka and R.E. Riman, *J. Am. Ceram. Soc.* **76**(10): 2649–2659 (1993).
13. M.M. Lencka and R.E. Riman, *Chem. Mater.* **7**(1): 18–25 (1995).
14. M.M. Lencka, A. Anderko, and R.E. Riman, *J. Am. Ceram. Soc.* **78**(10): 2609–2618 (1995).
15. M.M. Lencka, E. Nielsen, A. Anderko, and R.E. Riman, *Chem. Mater.* **9**(5): 1116–1125 (1997).
16. Film-Forming Hydrosols of Barium Titanate, Their Preparation and a Substrate Coated Therewith, US Pat. 2,841,503, July 1, 1958, B. Graham and G.D. Patterson.
17. K. Kajioshi, N. Ishizawa, and M. Yoshimura, *Jpn. J. Appl. Phys.* **30**(1B): L120–L123 (1991).
18. K. Kajioshi, N. Ishizawa, and M. Yoshimura, *J. Am. Ceram. Soc.* **74**(2): 369–374 (1991).
19. P. Bendale, S. Venigalla, J.R. Ambrose, E.D. Verink, Jr., and J.H. Adair, *J. Am. Ceram. Soc.* **76**(10): 2619–2627 (1993).
20. K. Kajioshi, M. Yoshimura, Y. Hamaji, K. Tomono, and T. Kasanami, *J. Mater. Res.* **11**(1): 169–183 (1996).
21. R. Bacsa, P. Ravindranathan, and J.P. Dougherty, *J. Mater. Res.* **7**(2): 423–428 (1992).
22. A.T. Chien, J.S. Speck, and F.F. Lange, *Mater. Res. Bull.* **12**(5): 1176–1178 (1997).
23. R.A. Laudise, *Chem. Eng. News* **28**: 30–43 (1987).
24. D.J. Marshall and R.A. Laudise, *Proc. Int. Conf. Crystl. Growth,* June 20–24, 1966, Boston, p. 557.
25. K. Yanagisawa and H. Kanai, *Jpn. J. Appl. Phys.* **36**(1–9B): 6031–6034 (1997).
26. W.J. Dawson, *Ceram. Bull.* **67**(10): 1673–1678 (1988).
27. M. Rafal, J.W. Berthold, N.C. Scrivner, and S.L. Grise, in *Models for Thermodynamic and Phase Equilibria Calculations*, S.I. Sandler, ed., Marcel Dekker, NY, 1995, pp. 601–670.
28. J.F. Zemaitis, Jr., D.M. Clark, M. Rafal, and N.C. Scrivner, *Handbook of Aqueous Electrolyte Thermodynamics*: Theory & Application. AIChE, NY, 1986.
29. M.M. Lencka and R.E. Riman, *Chem. Mater.* **5**(1): 61–70 (1993).
30. Environmental and Corrosion Simulation Programs (ESP/CSP), OLI Systems, Inc., Morris Plains, NJ, 1996.
31. M. Lencka, S.B. Cho, and R.E. Riman, June 2001.
32. H.C. Helgeson, D.H. Kirkham, and G.C. Flowers, *Am. J. Sci.* **281**: 1249–1428 (1981).
33. J.C. Tanger and H.C. Helgeson, *Am. J. Sci.* **288**: 19–98 (1988).
34. L.A. Bromley, AIChE J. **19**(2): 313–320 (1973).
35. K.S. Pitzer, *J. Phys. Chem.* **77**(2): 268–277 (1973).
36. G. Soave, *Chem. Eng. Sci.* **27**: 1197–1203 (1972).
37. H.P. Meissner in *Thermodynamics of Aqueous Systems with Industrial Application*, S.A. Newman, ed., Am. Chem. Soc. Symp. Ser., **133**: (1980), pp. 495–511.
38. E.L. Shock and H.C. Helgeson, *Geochim. Cosmochim. Acta* **52**: 2009–2036 (1988).
39. E.L. Shock, H.C. Helgeson, and D.A. Sverjensky, *Geochim. Cosmochim. Acta* **53**: 2157–2183 (1989).
40. D.D. Wagman, W.H. Evans, W.B. Parker, I. Halow, S.M. Bailey, and R.H. Schumm, NBS Technical Note 270/3–8, 1968–1982.
41. D.D. Wagman, W.H. Evans, W.B. Parker, R.H. Schumm, I. Halow, S.M. Bailey, K.L. Churney, and R.L. Nuttall, *J. Phys. Chem. Ref. Data* **11**: Suppl. No. 2 (1982).
42. M.W. Chase, Jr., C.A. Davies, J.R. Downey, Jr., D.J. Frurip, R.A. McDonald, and A.N. Syverud, *J. Phys. Chem. Ref. Data* **14**: Suppl. No. 1 (1985).
43. V.A. Medvedev, V.A. Bergman, L.V. Gurvich, V.S. Yungman, A.F. Vorobiev, and V.P. Kolesov, in *Thermicheskie Konstanty Veshchestv* (Thermal Constants of Substances), Vols. 1–10, V.P. Glushko, ed., Russian Academy of Sciences, Viniti, Moscow, USSR, 1962–1982.
44. R.A. Robie, B.S. Hemingway, and J.R. Fisher, Thermodynamic Properties of Minerals and Related Substances at 298.15 K and 1 Bar ($10^5$ Pascals) Pressure and at Higher Temperatures. U.S. Geological Survey Bulletin 1452, U.S. Government Printing Office, Washington, DC, 1995.
45. I. Barin in collaboration with F. Sauert, E. Schultze-Rhonhof, and W. Shu Sheng, *Thermochemical Data of Pure Substances*. VCH, NY, 1993.
46. A. Seidell, *Solubilities of Inorganic and Metal Organic Compounds*. 3e., 1, Van Nostrand Company, NY, 1940. Vol. 1.
47. W.F. Linke, and A. Seidell, *Solubilities of Inorganic and Metal-Organic Compounds*. 4e, American Chemical Society, Washington, DC, 1965, Vol. 2.
48. D.A. Sverjensky, in *Reviews in Mineralogy, Thermodynamic Modeling of Geologic Materials: Minerals, Fluids and Melts*, I.S.E. Carmichael and H.P. Eugster, eds., Mineralogical Society of America, Chelsea, MI, 1987, Vol. 17, pp.177–209.
49. M.M. Lencka and R.E. Riman, *Thermochim. Acta* **256**: 193–203 (1995).
50. D.A. Sverjensky, *Geochim. Cosmochim. Acta* **48**: 1127–1134 (1984).
51. D.A. Sverjensky and P.A. Molling, *Nature* **356**: 231–234 (1992).
52. W. Latimer, *The Oxidation State of Elements and Their Potentials in Aqueous Solutions*. 2e, Prentice-Hall, NY, 1952.
53. K. Osseo-Asare, F.J. Arriagada, J.H. Adair, in *Ceramic Transactions, Ceramic Powder Science* IIA, G.L. Messing, E.R. Fuller, Jr., H. Hausner eds. American Ceramic Society, Westerville, OH, 1988, Vol. I, p. 47.
54. A. Halliyal, U. Kumar, R.E. Newnham and L.E. Cross, *Am. Ceram. Soc. Bull.* **66**(4): 671–676, (1987).
55. T.R. Shrout and A. Halliyal, *Am. Ceram. Soc. Bull.* **66**(4): 704–711 (1987).
56. C.C. Hung, M.Sc. Thesis, Rutgers University, New Brunswick, NJ, 1990.
57. B. Gersten, M.M. Lencka, and R.E. Riman, in press.
58. S.B. Cho, M.M. Lencka, L.E. McCandlish, and R.E. Riman, in press.
59. J.O. Eckert, Jr., C.C. Hung-Houston, B.L. Gersten, M.M. Lencka, and R.E. Riman, *J. Am. Ceram. Soc.* **79**(11): 2929–2939 (1996).
60. P. Pinceloup, M. Oledzka, K. Mikulka-Bolen, M. Lencka, L. McCandlish, and R.E. Riman, June 2001.